Mitigating membrane fouling with sinusoidal spacers

Peng Xie, Lawrence C. Murdoch, David A. Ladner*

*Department of Environmental Engineering and Earth Sciences, Clemson University, Clemson, South Carolina 29625, USA,
Tel. +1 864-656-5572; email: ladner@clemson.edu (D.A. Ladner), Tel. +1 217-979-9878; email: pxie@g.clemson.edu (P. Xie),
Tel. +1 864-656-3438; email: lmurdoc@clemson.edu (L.C. Murdoch)*

ABSTRACT

Membrane fouling is a major drawback of reverse osmosis (RO) membrane filtration as it negatively affects the quantity and quality of the treated water and the lifespan of the membrane. Spacers play a pivotal role in the hydrodynamics of the membrane channel thus influencing membrane fouling. Building on our previous work (Xie et al., *Journal of Membrane Science*, 2014, 453:92–99) where a series of novel sinusoidal spacers were built, we investigate here the spacers' ability to mitigate foulant deposition onto membrane surfaces. Experiments were performed and a three-dimensional computational fluid dynamics (CFD) model was built. The results of experiments with humic acid and calcium ions (a surrogate foulant recipe) showed that certain sinusoidal spacers had less fouling than mesh spacers. Furthermore, the fouling on membranes diminished as the tortuosity (ratio of amplitude to wavelength of the sinusoidal pattern) increased. CFD simulations explored the development of fouling over time and the CFD results were compared with scanned images of fouled membranes. The simulation results matched well with the experimental results and suggested that wall shear stress alteration by the spacers could be a mechanism for fouling reduction.

Keywords: Reverse osmosis; Desalination; Fouling; Spacers; Computational fluid dynamics

1. Introduction

Fouling is a critical issue in reverse osmosis (RO) and other membrane filtration processes because it results in higher operational cost, shorter membrane lifespan, and less desirable permeate quality [1–6]. Studies on membrane fouling patterns often suggest that feed spacers play an important role in fouling development. Tran et al. [7] reported that fouling initially started along the feed spacer and then gradually encroached upon the rest of the clean membrane area. Gimmelshitein and Semiat [8] studied the flow in spacer-filled channels and found that the spacer exacerbated particle deposition near the mesh spacer filaments. Vrouwenvelder et al. [2] and Araújo et al. [9] studied the correlation between spacers and biofouling. They reported that biofouling was largely initiated on feed spacers and the pressure drop caused by biomass accumulation was much higher when the spacer was present. In seeking to advance membrane technology, surface modification and pretreatment methods are often discussed and employed [10,11] and the benefits of those efforts may be strengthened if spacer design is improved.

Several attempts to create new kinds of spacers to increase mass transfer or reduce pressure drop have been made [12–17]. However, compared with the conventional mesh spacers, those novel spacers usually mitigate the concentration polarization and improve flux at the cost of higher energy consumption [16–20]. In our previous study, we demonstrated that sinusoidal spacers had the potential to produce more permeate with lower pressure drop during seawater desalination because of a reduction in concentration polarization [21]. That work dealt only with

* Corresponding author.

non-adsorbing salts. In this study, we add adsorptive fouling into our experimental and modeling matrix to further evaluate the potential of sinusoidal spacers.

Both bench-scale experiments and three-dimensional computational fluid dynamics (CFD) models were employed in this work. Humic acid, which was used here as a model foulant, is one of the natural organic matters found in lakes, rivers and reservoirs and it is considered as a major foulant during membrane processes [22]. It has been recommended that humic acid be removed as much as possible in pre-treatment before RO [23]. The high potential for humic acid to cause flux reduction and the dark membrane surface coloring it creates makes it an ideal model foulant for the purpose of this study. Humic acid can form brownish gel-like chelates with multivalent ions on membrane surfaces [24,25]. Calcium-humate can cause significant irreversible flux decline [26], though solution pH, ionic strength, and multivalent ion concentration are important in determining the magnitude of humic acid adsorption during membrane filtration [27,28].

CFD is a widely used technology when it comes to spacer design [9,13,17,29–33]. A variety of studies using 2D [14,20,30,34,35] or 3D [16,32,36–38] CFD models to investigate and improve membrane spacers is available in the literature. Analysis of adsorptive membrane fouling by CFD is challenging because both the hydrodynamic (i.e., velocity, concentration polarization) and thermodynamic (i.e., humic acid–membrane interactions) conditions need to be considered. The Langmuir model has been used in predicting humic acid adsorption during membrane filtration [27,28,39], which is a good model to start with when dealing with adsorption [23], but hydrodynamics need to be considered in order to simulate adsorptive fouling on RO membranes in crossflow mode. Most current mathematical models are empirical [28,40,41] and do not fully consider hydrodynamics. In this study, simulations investigate the influence of both thermodynamics and hydrodynamics on adsorptive membrane fouling in a crossflow environment when different spacers are used.

2. Materials and methods

2.1. Experimental setup

Experiments were performed using the same spacers described in our previous publication [21]. They were made with PolyJet 3D printing using VeroClear material (Stratasys, Eden Prairie, Minnesota, USA). A 3D rendering of one sinusoidal spacer is shown in Fig. 1 with the detailed drawing, dimensions, and fluid flow directions depicted in Fig. 2. Five models of RO spacer channels with varying geometry were created for analysis (Fig. 3). The channels have a wall geometry described by

$$y = a\sin\left(\frac{2\pi x}{L}\right) \tag{1}$$

where a is the amplitude and L is the wavelength. The amplitude a was either 3 or 6 mm, and L was either 12 or 24 mm. This generated four channel geometries, which will be referred to as $3\sin(\pi/12)$, $3\sin(\pi/6)$, $6\sin(\pi/12)$, and $6\sin(\pi/6)$.
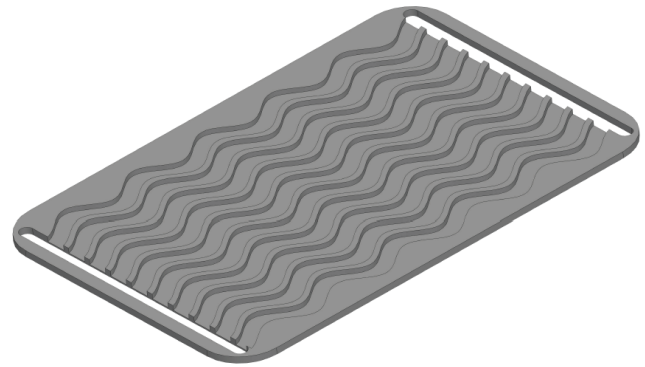

Fig. 1. Oblique view of a representative sinusoidal spacer built for experiments. This spacer has the $3\sin(\pi/12)$ geometry. This is the same spacer view as shown in our previous work [21].
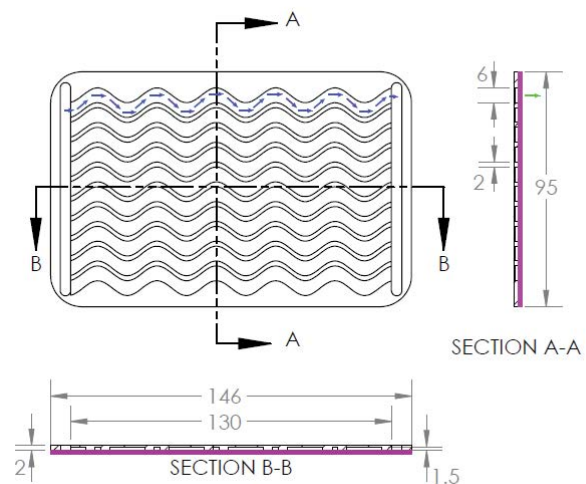

Fig. 2. Plan and section views of a representative sinusoidal spacer. As with Fig. 1, this spacer has the $3\sin(\pi/12)$ geometry. Blue arrows indicate the water flow path. Dimensions are in mm. These are the same dimension as the spacers from our previous work [21].

Channels were created by offsetting the sinusoidal wall geometry by 6 mm normal to the y direction. The cross-sectional geometry of the channel normal to the y direction was a 1.5 mm by 6 mm rectangle, with the membrane lying along one of the 6 mm sides. A straight channel was also modeled, representing the non-sinusoidal control. The direct inlet-to-outlet distance was 130 mm, yielding an active membrane area of 7.8 cm^2 for a single membrane channel, regardless of the amplitude and wavelength of the sinusoid.

The RO unit (Fig. 4) used a SEPA II membrane cell (GE Osmonics; now Sterlitech). Additional details about the RO unit were previously reported [21]. Each sinusoidal spacer and the straight-channel spacer was tested in this unit using a SWC5 (Hydranautics, Oceanside, California, USA) membrane coupon cut from a 4-inch spiral-wound element. For comparison, one experimental set was performed using the 65 mil mesh feed spacer that is a standard accessory of
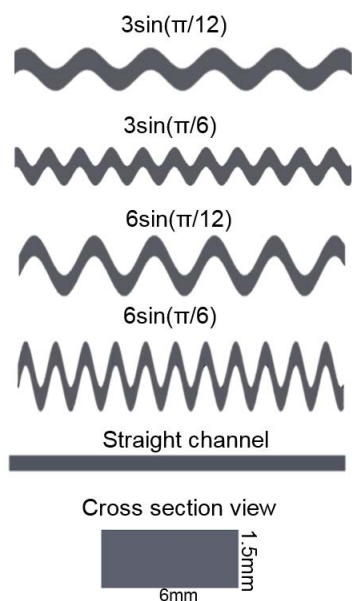
Fig. 3. Geometries of sinusoidal channels. The overall length of each channel is 130 mm. The cross-sectional view (bottom) applies to all geometries. These are the same geometries as studied in our previous work [21].
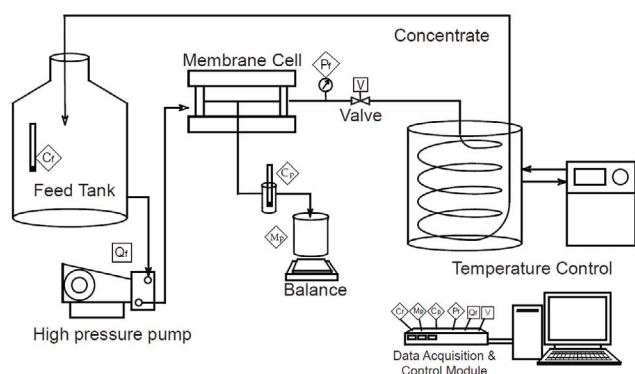

Fig. 4. Bench-scale RO membrane test setup. Square symbols denote controls (V for needle valve actuator voltage and Q_f for the feed flow rate control). Diamond symbols denote data acquisition points (C_f for feed concentration, M_p for permeate mass, C_p for permeate concentration, and P_f for feed pressure). This is the same test setup as used in our previous work [21].

the SEPA II cell. (Though 65 mil is the spacer designation, its actual thickness was measured to be 1.5 mm [60 mil]).

Before the experiments, each membrane coupon was soaked with deionized (DI) water overnight. For the first hour of each experiment the system was operated with DI water to stabilize the membrane and obtain the clean-water flux to calculate the hydraulic permeability of the membrane coupon. At the end of the first hour, the DI water was replaced by 10 L of fouling solution, which consisted of humic acid (catalog number 198763, lot number 7078J, MP Biomedicals, Santa Ana, California, USA) (30 mg/L), calcium chloride (30 mmol/L) and sodium bicarbonate (1 mmol/L). The pH of the fouling solution was 6.0. The pressure was set to 600 psi (4,140 kPa) and the crossflow velocity was set

to 0.15 m/s; these are typical values for industrial RO operation. The fouling solution combined with the chosen operating conditions resulted in foulant accumulation that was fast enough to expedite the experiments, but slow enough to allow observation of the gradual buildup of material.

Humic acid was chosen for this work because of its strong binding with the membrane (especially in the presence of calcium) and for its dark color. The color allowed us to visualize the locations of greatest foulant deposition. The most egregious fouling in full-scale RO applications is usually due to biofilm development, but a conditioning film has been recognized as a precursor to the biofilm [42]. This study investigates that initial deposition of organic matter. To shorten the time-frame for experiments, the humic acid concentrations used here are much higher than would be seen in practice because pretreatment is employed in RO plants to minimize organic-matter concentrations.

Two sets of experiments with the same solution but different durations were performed. The first set of experiments was terminated when 5 L of permeate was collected (around 3.5 h). The average value of permeate flux over the last 3 min was used to compare with DI water flux obtained at the beginning of the experiment to calculate the flux decline. The purpose was to examine how the flux decline was affected by the different sinusoidal spacers. In contrast, the second set of experiments were terminated after 1 L of permeate was collected. This stopping point was determined via trial and error in order to find a volume of permeate that generated membrane coupons where the local variation of fouling severity was clearly visible. The membrane coupons after this set of fouling experiments were dried and digitized using an optical scanner (MP C4503, Ricoh, Malvern, Pennsylvania, USA) to create fouled-membrane images. All experiments for flux decline were performed in triplicate, meaning that three different membrane coupons were tested for each spacer.

2.2. Model development

The purpose of the computer simulations was to study hydrodynamic and concentration profiles that are difficult to observe via lab experiments. In our previous work, 3D models were created to mimic the laboratory conditions [21]. The models were calibrated with salt–water experimental data to ensure that the flux predicted by the model simulations matched the experimental results. In the current effort, the models were extended to include adsorptive fouling. The fouling models were calibrated to ensure that the spatial distributions of adsorbed material in the simulations mimicked the distributions seen in the experiments. Having these models that accurately represented both the flux and the foulant spatial distribution, we could then evaluate the details of the hydrodynamic environment that led to or mitigated fouling.

3D simulations were performed using Comsol Multiphysics 4.2a on the Palmetto Cluster, Clemson University's primary high-performance computing resource. The mesh consisted of triangular elements on the membrane surface and on the opposite wall, which were swept through the domain to create triangular prisms of equal thickness (Fig. 5). Mesh density was evaluated by comparing results for a sinusoidal channel $6\sin(\pi/6)$ with 380 elements/mm^3 (456,400
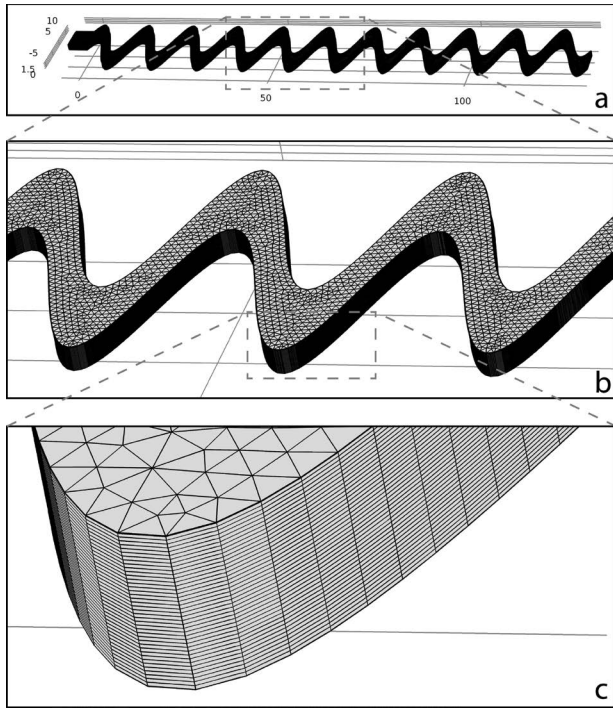
Fig. 5. Mesh scheme of the sinusoidal spacer *6sin(π/6)*. The membrane is on the bottom face in this view. (a) Full extent of model with numbers indicating mm distances. (b) Inset showing three periods of the sinusoidal shape. (c) Inset showing mesh vertices on the flat wall and throughout the channel.

elements) to results from a simulation with a mesh density that was roughly twice as large (745 elements/mm³). The results were essentially the same, but the execution times were much different so the coarser mesh was used. In some cases, coarser meshes had convergence problems, so mesh densities were tuned for each model to identify a density that minimized execution time while ensuring consistent convergence. This resulted in mesh densities in the range of 360–480 elements/mm³.

3D models were designed to simulate the development of a foulant layer on the membrane surface over time under given thermo- and hydrodynamic conditions. The highest Reynold's number was 907, found in channel 6sin(π/6), therefore the laminar flow module in Comsol was used for the hydrodynamic simulation. The models did not take into account changes in the cross-sectional area of the flow channel due to fouling. The velocity distribution and salt concentration remained constant and were solved at steady state. The velocity distribution was then used by the foulant transport model to complete the simulation of the fouling process on the membrane surface. The foulant layer development was modeled as a non-equilibrium adsorption process.

2.3. Theoretical description

Both steady state and time-dependent simulations were performed in this study. In the first simulation step, a steady-state simulation was used to solve for velocity, pressure and salt concentration using

$$\nabla \cdot \mathbf{u} = 0 \tag{2}$$

$$\rho \mathbf{u} \cdot \nabla \mathbf{u} = -\nabla P + \nabla \cdot \mu \left[\nabla \mathbf{u} + \left(\nabla \mathbf{u} \right)^T \right] \tag{3}$$

$$\mathbf{u} \nabla c = D_c \nabla^2 c \tag{4}$$

where $\mathbf{u}$ is the fluid velocity vector, ρ is the density, P is the pressure, μ is the dynamic viscosity, c is the salt concentration, and D_c is the diffusion coefficient of salt in water.

Water flow across the membrane was included by using the boundary condition

$$u_m = A \left(\Delta p - a_{\text{osm}} c_w \right) \tag{5}$$

where u_m is the volumetric flux of the permeate normal to the boundary, c_w is the salt concentration at the membrane surface, A is the water permeability of the membrane, Δp is the pressure difference between feed side and permeate side and a_{osm} is the osmotic coefficient. The upstream boundary condition specified the inflow velocity as 0.15 m/s, whereas the pressure on the downstream boundary was specified as 600 psi (4140 kPa) to correspond with the experiments. Other flow boundaries were no flow. The upstream concentration was specified as 0.001 mol/m³, and the downstream condition assumed no diffusive flux, but the advective outflow was unrestricted. The concentration boundary condition on the membrane specified no mass flux.

The fluid velocity distribution obtained from the first step was used for the second step. In the second step, chemical transport was solved with the convective diffusion equation (Eq. (6)).

$$\frac{dc_f}{dt} = D_f \nabla^2 c_f - \mathbf{u} \nabla c_f \tag{6}$$

Simultaneously with chemical transport, the adsorption of foulant was solved. This fouling model resembles Langmuir kinetics with an additional term describing desorption caused by fluid shear. It has the following assumptions [28,43]:

- The physical and chemical properties of the membrane surface are homogenous.
- There is no interaction among solutes, nor among adsorbates.
- The foulant only forms a monolayer on the membrane surface.
- Fluid shear causes desorption in addition to that which would occur in a stagnant system.

The above four assumptions are built into Eq. (7):

$$\frac{dc_s}{dt} = k_1 \left(1 - \frac{c_s}{c_{\text{se}}} \right) c_f - \frac{k_2 c_s}{c_{\text{se}}} - R_s \tag{7}$$

where c_f is the foulant concentration in the bulk fluid, D_f is the diffusion coefficient for foulant in water, c_s is the foulant concentration on the membrane surface (per unit area), c_{se} is the maximum surface concentration of foulant (per unit area), and k_1 and k_2 are the adsorption and desorption rate

constants, respectively. R_s is the desorption rate caused by shear stress on the membrane.

The values of $D_f = 2.2 \times 10^{-11}$ m² s⁻¹, $k_1 = 1.37 \times 10^{-4}$ m s⁻¹, $k_2 = 1.05 \times 10^{-11}$ mol m⁻² s⁻¹, and $c_{se} = 0.105$ µg cm² are from the study of Jones and O'Melia [28] under conditions of pH = 8 and ionic strength = 0.001 M. D_f and c_{se} were reported directly by Jones and O'Melia [28], and k_1 and k_2 were calculated by the following equation:

$$k_2 = \frac{R_0 \theta^2 D_f}{c_{se}} \qquad (8)$$

$$k_1 = \frac{k_2}{\theta} \qquad (9)$$

R_0 (9,000) and θ (7.65 × 10⁻⁸ mol m⁻³) were derived from the values reported by Jones and O'Melia [28], who studied humic acid adsorption on ultrafiltration membranes. We recognize that the adsorption parameters may vary between that and this work because the membrane materials were different, the humic acid was from a different supplier, and the pH was different. Nevertheless, these values are the best available published estimates of the parameters relevant to our experiments and serve as a starting point for our simulations.

The additional desorption due to fluid shear (R_s) is described by:

$$R_s = \begin{cases} 0; & c_s = 0 \\ k_3 \tau f(\tau, b); & c_s > 0 \end{cases} \qquad (10)$$

where k_3 is a constant and $f(\tau, b)$ is a smoothed unit step function of half width b defined by:

$$f(\tau, b) = \begin{cases} 0, & \tau < 0 \\ 0.5 + a_1 \omega - a_2 \omega^3 + a_3 \omega^5, & 0 \le \tau \le 2b \\ 1, & \tau > 2b \end{cases} \qquad (11)$$

where $\omega = \dfrac{\tau - b}{b}$, $b = 2,000$, $a_1 = 0.9375$, $a_2 = 0.625$, and $a_3 = 0.1875$. The desorption rate (10) is first-order in τ when $\tau > 2b$, and is zero-order in c_s. The R_s was introduced because the conventional Langmuir kinetics model does not include the impact of the shear force. The reported values of the terms within R_s (k_3 and b) were determined by trial and error, where k_3 and b were adjusted until the simulations produced foulant distributions similar to the images from the experiments. The step function (11) was included to improve numerical convergence. This gave $k_3 = 5 \times 10^{-17}$ mol/m² and $b = 2,000$ 1/s.

3. Results and discussion

Results are presented in three parts. First, we verify that sinusoidal spacers affect the level of fouling in laboratory tests. We evaluate fouling mitigation in light of longitudinal pressure drop to determine how the gain in performance is offset by the increase in applied energy. Second, we use the results from computational models to evaluate the kinetics of foulant accumulation. Third, we validate the model using the spatial distribution of foulant deposition from the experimental results. This helps elucidate the mechanisms at play for sinusoidal spacers in RO.

3.1. Flux decline percentage and pressure drop

The flux decline percentage was measured as:

$$\alpha = \frac{J_{DI} - J_f}{J_{DI}} \times 100\% \qquad (12)$$

where J_{DI} is the average flux of the final three minutes of the DI water run and J_f is the average flux of the final three minutes of the fouling experiment. Flux decline percentage was used as the criterion to evaluate the fouling mitigation performance of each spacer.

Among the sinusoidal spacers, the values of J_{DI} were similar to one another, while J_f was altered by the different spacer patterns (Fig. 6). By increasing the amplitude or reducing the wavelength of the sinusoidal wave, J_f, was increased. The mesh spacer showed a higher J_{DI} because it probably had a larger active membrane area, but it should be noted that the active membrane areas for all sinusoidal spacers and the straight spacer were the same.

The flux decline observed in experiments was compared with the longitudinal pressure drop of the various channels evaluated by computational simulations (Fig. 7). The sinusoidal spacers and mesh spacer all exhibited lower flux decline percentages than the straight spacer. In addition, the flux decline of the sinusoidal spacer 6sin(π/6) (14%) was less
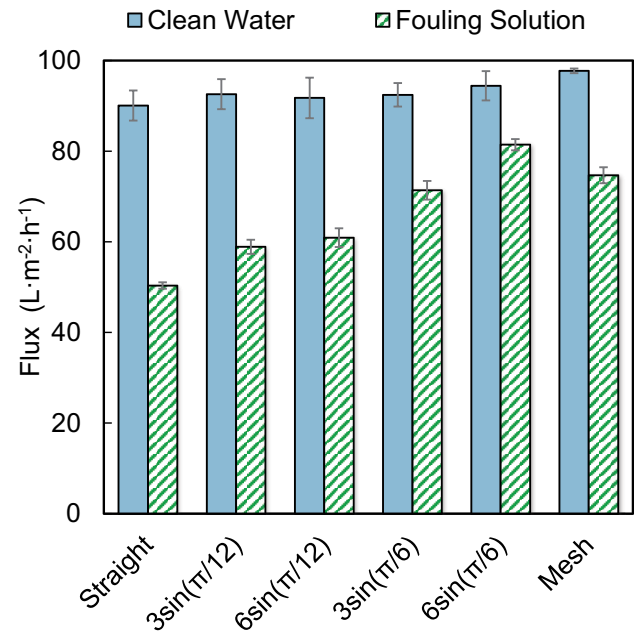

Fig. 6. DI water flux compared with final flux from the experiments. The blue bars indicate the clean-water test and the hatched bars the fouling solution tests. Bar heights are the averages of triplicate tests. Error bars represent the standard deviation.
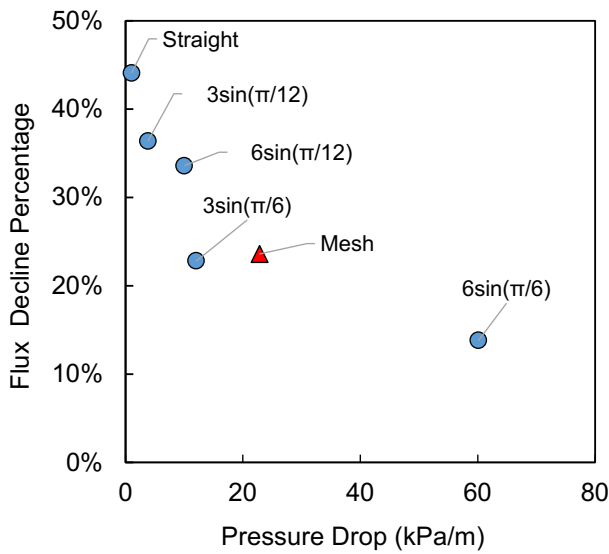
Fig. 7. Flux decline percentage (from the experiments) vs. the pressure drop (from the simulations) under equal feed flow rate (crossflow velocity entering the channels was 0.15 m/s) and equal concentrate pressure (600 psi, 4,140 kPa).

than the conventional mesh spacer (24%), which demonstrated an improvement in fouling mitigation. Meanwhile the spacer 3sin(π/6) showed a similar flux decline (23%) as the mesh spacer. The smallest pressure drop was from the simulation of the straight channel (1 kPa/m) and the largest pressure drop was from the channel formed by 6sin(π/6) (60 kPa/m). The mesh spacer simulation showed the second largest pressure drop (23 kPa/m), which was greater than from the 3sin(π/6) spacer simulation (12 kPa/m). The same flow rate was used in the simulations, so the pressure drop is proportional to the energy consumed by viscous dissipation. These data show that the 3sin(π/6) spacer was capable of achieving a similar level of flux decline, and therefore fouling mitigation, with less energy consumption than the mesh spacer.

The flux decline vs. pressure drop results shown in Fig. 7 demonstrate that fouling control improves when energy consumption increases (i.e., increase in pressure drop). An important follow-up issue is whether the fouling control is worth the greater energy cost. One way to analyze this is to convert the flux decline numbers into energy terms. The resistance of the fouling layer (R_f) affects the flux (u) according to the following equation:

$$u = \frac{\Delta p}{\mu\left(R_m + R_f\right)} \tag{13}$$

where μ is viscosity and R_m is membrane resistance. Eq. (13) is similar to Eq. (5), but without the osmotic pressure term. The ensuing analysis was repeated after adding osmotic pressure effects into Eq. (13), but for all reasonable levels of osmotic pressure (up to half the applied pressure) the results were similar.

Using the measured clean-water flux (90 L m^{-2} h^{-1} or 2.5 × 10^{-5} m/s) and applied pressure (4,140 kPa) with a

viscosity typical of water (0.001 Pa s) in Eq. (13), R_m was calculated to be 1.66 × 10^{14} m^{-1}. Using this membrane resistance and solving for R_f gives 1.3 × 10^{14}, 0.97 × 10^{14}, 0.82 × 10^{14}, 0.47 × 10^{14}, 0.49 × 10^{14}, and 0.27 × 10^{14} m^{-1} for the straight, 3sin(π/12), 6sin(π/12), 3sin(π/6), mesh, and 6sin(π/6) spacers, respectively. This result shows that the resistance caused by the foulant ranges from 0.2 to 0.8 of the resistance from the membrane itself.

From Eq. (13) we can write an expression for the pressure increase that would be caused by fouling: $\Delta p_f = u_c \mu R_f$, where u_c is the clean-water flux. The total excess pressure needed to operate the membrane with spacers at the clean-water flux was determined as the sum of Δp_f and the longitudinal pressure drop created by the spacers. Here the longitudinal pressure drop for a 6-m-long distance was used; this is roughly six elements in series, which is typical of a full-scale application. All of the energy expended in this system is expended in the form of pressure drop; thus analysis of pressure drop is simultaneously an analysis of energy.

The results indicate that the pressure increase caused by fouling is larger than the longitudinal pressure drop, although the values are similar in the 6sin(π/6) case (Fig. 8). The total excess pressure for two of the sinusoidal channels, 3sin(π/6) and 6sin(π/6) was less than that for the conventional mesh spacer.

3.2. Foulant accumulation on membrane surface

The simulated foulant accumulation was similar among all spacers when the effects of the wall shear stress on the foulant accumulation were ignored ($R_s = 0$; Fig. 9a). However, the rate and total mass of foulant accumulation were changed by including the effects of wall shear stress
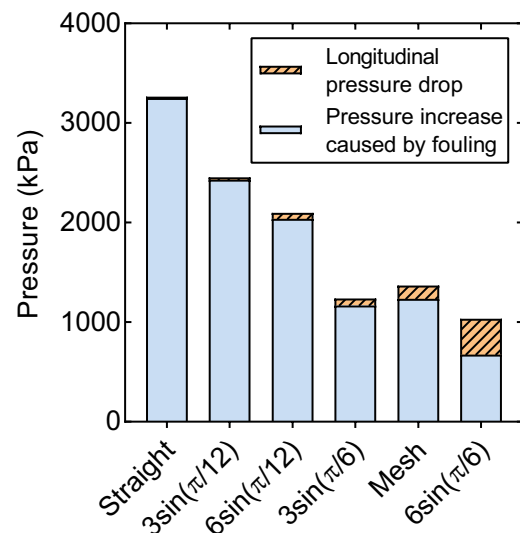

Fig. 8. Simulation results showing pressure requirements for various spacers. Longitudinal pressure drop is reported for 6 m of spacer length, similar to a typical full-scale application. The pressure increase required by fouling is the additional pressure that would be needed to produce the same flux with a fouled membrane as with a clean membrane, assuming the flux decline percentages shown in Fig. 7.
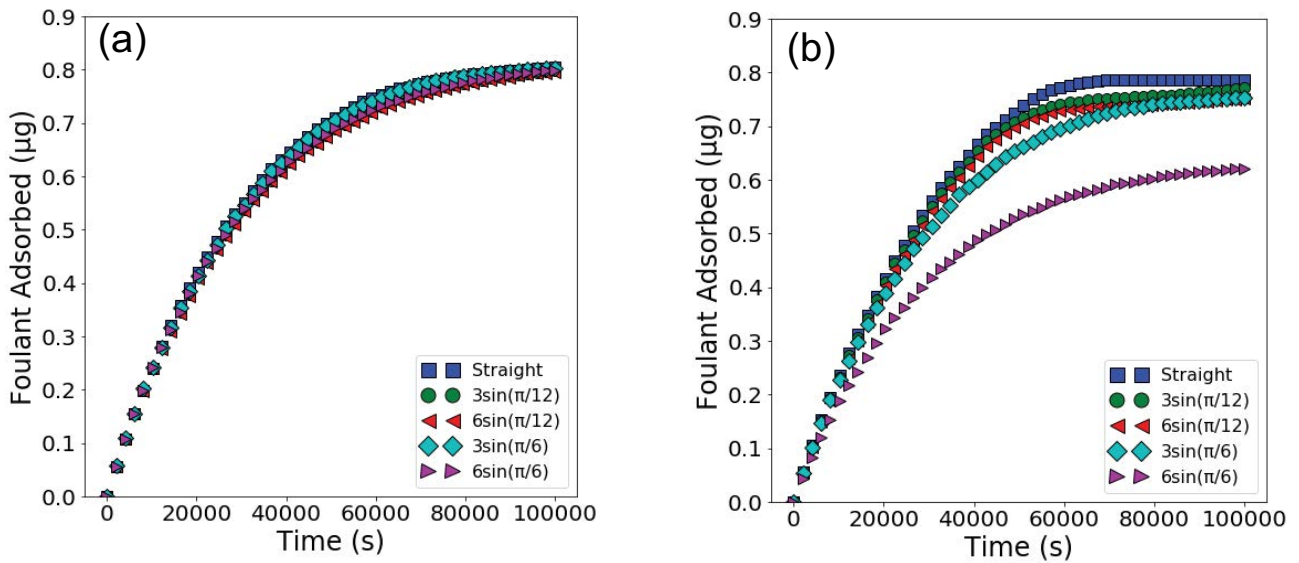
Fig. 9. Simulation results of total mass of foulant adsorbed on the membrane surface over time using different spacers when (a) the shear stress was ignored ($R_s = 0$) and (b) shear stress was included (R_s follows Eq. (10)). The crossflow velocity was 0.15 m/s and applied pressure was 600 psi (4,140 kPa).

in the simulations ($R_s > 0$; Fig. 9b). The results show that the total mass of foulant that accumulated using the highest-tortuosity (a/L in Eq. 1) spacer was less than the mass accumulated on the other spacers (Fig. 9b). This is consistent with the experimental observations (Fig. 7) where flux decline with the highest-tortuosity spacer was less than that with the other spacers. This suggests that variations in wall shear stress created by the spacer could be reducing fouling and its associated flux decline.

3.3. Fouling distribution

The foulant distributions predicted by the simulations captured important details of the fouling pattern observed in the experiments (Fig. 10). The simulation images were chosen at $t = 40,000$ s because the foulant patterns were clear at that time. In the straight channel, the foulant concentration was even in the direction perpendicular to the flow, and it decreased along the flow direction. The simulations indicated slightly greater foulant concentration along the walls (0.1 mg/cm²) than in the middle of the straight channel (0.085 mg/cm²), but this difference would be undetectable in our experimental data. In sinusoidal spacers, the foulant accumulated in the concave and convex locations, and it was sparse along the axis of the channel. Comparing with the shear stress distribution on the membrane surfaces obtained from simulations (Fig. 11), it is apparent that less fouling was observed in the experiments in regions of higher shear. These results suggest that relatively high wall shear stress suppresses the concentration of foulant along the axis of the tortuous channel (Fig. 10), and it explains the reduction in flux decline observed in the experiments (Fig. 6).

Variations in wavelength and amplitude of the sinusoidal channels had a significant effect on the shear stress distribution and magnitude. The shear stress in the straight channel was the smallest and uniformly distributed while
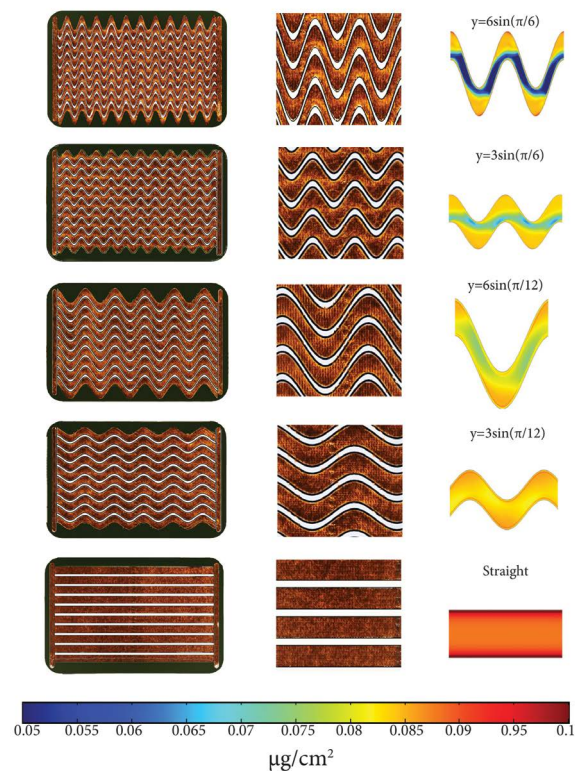

Fig. 10. Comparison between fouled membrane images for simulations and experiments. The whole membrane coupon with spacer wall is shown on the left; an enlarged view of the membrane coupon is in the middle (with contrast adjusted to increase clarity); and the simulated foulant distribution on the membrane surface is shown on the right. The foulant distributions were taken at $t = 40,000$ s from the simulation that included the ability of wall shear stress to suppress fouling. Bar scale shows foulant concentration in µg/cm².
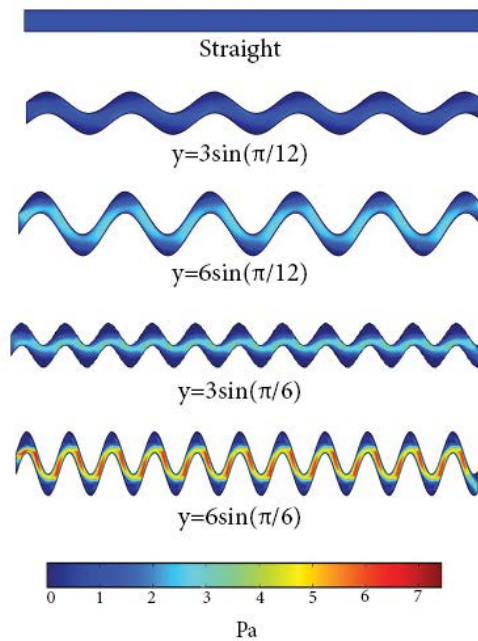
Fig. 11. Shear stress distribution on membrane surface from numerical simulations.

an appreciable variation of shear stress distribution was observed in the sinusoidal channels. The channels with higher tortuosity (higher magnitude and/or frequency) generated more turbulent flow patterns, which was reflected by an overall increase in shear stress that reduced fouling. However, the trade-off is that the pressure drop for the more tortuous channels was higher. The optimal channel geometry is one that strikes a balance: it is tortuous enough to help reduce fouling, yet not so tortuous that it greatly exacerbates pressure drop.

4. Conclusion

Building on and extending our previous work with concentration polarization reduction [21], the ability of sinusoidal spacers to reduce foulant deposition was tested and compared with a conventional mesh spacer and a straight spacer. Sinusoidal spacers were capable of decreasing deposition on the membrane surface and maintaining relatively high fluxes. Experiments showed that foulant deposition was greatest in low-velocity regions where the spacer curvature was high, but it was reduced along a sinuous band where the flow velocity and wall shear stress were high. Numerical simulations that include the effect of wall shear stress on foulant accumulation predict the patterns observed in the experiments (Fig. 10), and suggest that the beneficial mechanism of the sinusoidal spacers is their ability to reduce fouling by increasing wall shear stress. This increase in wall shear stress comes at a penalty of increased longitudinal pressure drop and energy loss; however, the benefit of suppressing foulant accumulation offsets the increased energy loss for certain spacer designs, resulting in a net reduction in the total energy required to produce a unit volume of permeate (Fig. 8).

The novelty of this work is that it describes a methodology for identifying membrane spacer designs that considers both the energy loss along the spacer and the energy loss during flow through the membrane in the presence of fouling. This approach identified a channel design [$3\sin(\pi/6)$ sinusoid] that produced permeate with less energy consumption than conventional spacers. The approach was also able to screen other spacer designs with relatively poor performance. This finding suggests that sinusoidal spacers (or similar novel designs yet to be developed) may be a viable approach for economically reducing fouling in membrane processes, and the method used here appears to be well suited to optimizing future designs.

Symbols

A — Hydraulic permeability of the membrane, m/(s Pa)
a_{osm} — Osmotic pressure coefficient, Pa m³/mol
c — Foulant concentration in the bulk, mg/L
c_w — Foulant concentration near the membrane, mg/L
c_s — Foulant concentration being adsorbed to the membrane, mg/m²
c_{se} — Equilibrium foulant concentration that can be adsorbed to the membrane, mg/m²
k_1 — Adsorption coefficient, 1/s
k_2 — Desorption coefficient
k_3 — Constant
R_0 — Ratio of diffusion-controlled adsorption characteristic time, 9,000
R_s — Desoprtion rate due to the shear stress on the membrane
R_m — Membrane resistance, m⁻¹
R_f — Foulant layer resistance, m⁻¹
D — Diffusivity, m²/s
E — Energy consumption per 1 m³ permeate under equal pressure drop condition, kJ/m³
n — Normal direction of boundary
p — Pressure in the channel, kPa
Δp — Pressure difference across the membrane, kPa
u — Velocity magnitude, m/s
u_m — Permeate flux, m/s
J_{DI} — Averaged flux during the DI water run, LMH
J_f — Averaged flux at the end of fouling experiment, LMH
Y — Recovery rate

Greek

$\Delta\pi$ — Osmotic pressure, Pa
μ — Viscosity of water, Pa s
ρ — Density of water, kg/m³

τ   —   Shear stress, Pa
α   —   Flux decline ratio

References

[1] J.S. Vrouwenvelder, J.W.N.M. Kappelhof, S.G.J. Heijman, J.C. Schippers, D. van der Kooij, Tools for fouling diagnosis of NF and RO membranes and assessment of the fouling potential of feed water, Desalination, 157 (2003) 361–365.

[2] J.S. Vrouwenvelder, D.A. Graf von der Schulenburg, J.C. Kruithof, M.L. Johns, M.C.M. van Loosdrecht, Biofouling of spiral-wound nanofiltration and reverse osmosis membranes: a feed spacer problem, Water Res., 43 (2009) 583–594.

[3] D. Jermann, W. Pronk, R. Kagi, M. Halbeisen, M. Boller, Influence of interactions between NOM and particles on UF fouling mechanisms, Water Res., 42 (2008) 3870–3878.

[4] T. Lin, Z. Lu, W. Chen, Interaction mechanisms and predictions on membrane fouling in an ultrafiltration system, using the XDLVO approach, J. Membr. Sci., 461 (2014) 49–58.

[5] L. Song, Flux decline in crossflow microfiltration and ultrafiltration: mechanisms and modeling of membrane fouling, J. Membr. Sci., 139 (1998) 183–200.

[6] N. Lee, G. Amy, J.-P. Croué, H. Buisson, Identification and understanding of fouling in low-pressure membrane (MF/UF) filtration by natural organic matter (NOM), Water Res., 38 (2004) 4511–4523.

[7] T. Tran, B. Bolto, S. Gray, M. Hoang, E. Ostarcevic, An autopsy study of a fouled reverse osmosis membrane element used in a brackish water treatment plant, Water Res., 41 (2007) 3915–3923.

[8] M. Gimmelshtein, R. Semiat, Investigation of flow next to membrane walls, J. Membr. Sci., 264 (2005) 137–150.

[9] P.A. Araújo, D.J. Miller, P.B. Correia, M.C.M. Van Loosdrecht, J.C. Kruithof, B.D. Freeman, D.R. Paul, J.S. Vrouwenvelder, Impact of feed spacer and membrane modification by hydrophilic, bactericidal and biocidal coating on biofouling control, Desalination, 295 (2012) 1–10.

[10] G.-d. Kang, Y.-m. Cao, Development of antifouling reverse osmosis membranes for water treatment: a review, Water Res., 46 (2012) 584–600.

[11] Y. Baek, J. Yu, S.-H. Kim, S. Lee, J. Yoon, Effect of surface properties of reverse osmosis membranes on biofouling occurrence under filtration conditions, J. Membr. Sci., 382 (2011) 91–99.

[12] J. Balster, D.F. Stamatialis, M. Wessling, Membrane with integrated spacer, J. Membr. Sci., 360 (2010) 185–189.

[13] J. Schwinge, D.E. Wiley, A.G. Fane, Novel spacer design improves observed flux, J. Membr. Sci., 229 (2004) 53–61.

[14] J. Schwinge, D.E. Wiley, A.G. Fane, R. Guenther, Characterization of a zigzag spacer for ultrafiltration, J. Membr. Sci., 172 (2000) 19–31.

[15] W. Li, K.K. Chen, Y.-N. Wang, W.B. Krantz, A.G. Fane, C.Y. Tang, A conceptual design of spacers with hairy structures for membrane processes, J. Membr. Sci., 510 (2016) 314–325.

[16] F. Li, W. Meindersma, A.B. de Haan, T. Reith, Novel spacers for mass transfer enhancement in membrane separations, J. Membr. Sci., 253 (2005) 1–12.

[17] F. Li, G.W. Meindersma, A.B. de Haan, T. Reith, Optimization of non-woven spacers by CFD and validation by experiments, Desalination, 146 (2002) 209–212.

[18] G. Schock, A. Miquel, Mass transfer and pressure loss in spiral wound modules, Desalination, 64 (1987) 339–352.

[19] J. Fárková, The pressure drop in membrane module with spacers, J. Membr. Sci., 64 (1991) 103–111.

[20] A. Subramani, S. Kim, E.M.V. Hoek, Pressure, flow, and concentration profiles in open and spacer-filled membrane channels, J. Membr. Sci., 277 (2006) 7–17.

[21] P. Xie, L.C. Murdoch, D.A. Ladner, Hydrodynamics of sinusoidal spacers for improved reverse osmosis performance, J. Membr. Sci., 453 (2014) 92–99.

[22] R. Ikan, Aquatic humic substances—influence on fate and treatment of pollutants, Org. Geochem., 15 (1990) 219.

[23] Z. Domany, I. Galambos, G. Vatai, E. Bekassy-molnar, Humic substances removal from drinking water by membrane filtration, Desalination, 145 (2002) 333–337.

[24] M.F.A. Goosen, S.S. Sablani, H. Al-Hinai, S. Al-Obeidani, R. Al-Belushi, D. Jackson, Fouling of reverse osmosis and ultrafiltration membranes: a critical review, Sep. Sci. Technol., 39 (2005) 2261–2297.

[25] M.R. Esfahani, H.A. Stretz, M.J.M. Wells, Comparing humic acid and protein fouling on polysulfone ultrafiltration membranes: adsorption and reversibility, J. Water Process Eng., 6 (2015) 83–92.

[26] A.I. Schäfer, M. Mastrup, R.L. Jensen, Particle interactions and removal of trace contaminants from water and wastewaters, Desalination, 147 (2002) 243–250.

[27] E. Salehi, S.S. Madaeni, Adsorption of humic acid onto ultrafiltration membranes in the presence of protein and metal ions, Desalination, 263 (2010) 139–145.

[28] K.L. Jones, C.R. O'Melia, Protein and humic acid adsorption onto hydrophilic membrane surfaces: effects of pH and ionic strength, J. Membr. Sci., 165 (2000) 31–46.

[29] J. Schwinge, P.R. Neal, D.E. Wiley, D.F. Fletcher, A.G. Fane, Spiral wound modules and spacers: review and analysis, J. Membr. Sci., 242 (2004) 129–153.

[30] S. Ma, L. Song, Numerical study on permeate flux enhancement by spacers in a crossflow reverse osmosis channel, J. Membr. Sci., 284 (2006) 102–109.

[31] L. Song, S. Ma, Numerical studies of the impact of spacer geometry on concentration polarization in spiral wound membrane modules, Ind. Eng. Chem. Res., 44 (2005) 7638–7645.

[32] M. Shakaib, S.M.F. Hasani, M. Mahmood, CFD modeling for flow and mass transfer in spacer-obstructed membrane feed channels, J. Membr. Sci., 326 (2009) 270–284.

[33] G.A. Fimbres-Weihs, D.E. Wiley, Numerical study of mass transfer in three-dimensional spacer-filled narrow channels with steady flow, J. Membr. Sci., 306 (2007) 228–243.

[34] A.L. Ahmad, K.K. Lau, Impact of different spacer filaments geometries on 2D unsteady hydrodynamics and concentration polarization in spiral wound membrane channel, J. Membr. Sci., 286 (2006) 77–92.

[35] S. Ma, L. Song, S.L. Ong, W.J. Ng, A 2-D streamline upwind Petrov/Galerkin finite element model for concentration polarization in spiral wound reverse osmosis modules, J. Membr. Sci., 244 (2004) 129–139.

[36] S. Karode, A. Kumar, Flow visualization through spacer filled channels by computational fluid dynamics I.: pressure drop and shear rate calculations for flat sheet geometry, J. Membr. Sci., 193 (2001) 69–84.

[37] R. Iwatsu, K. Ishii, T. Kawamura, K. Kuwahara, J.M. Hyun, Numerical simulation of three-dimensional flow structure in a driven cavity, Fluid Dyn. Res., 5 (1989) 173–189.

[38] W.S. Kim, J.K. Park, H.N. Chang, Mass transfer in a three-dimensional net-type turbulence promoter, Int. J. Heat Mass Transfer, 30 (1987) 1183–1192.

[39] S.M.G. Demneh, B. Nasernejad, H. Modarres, Modeling investigation of membrane biofouling phenomena by considering the adsorption of protein, polysaccharide and humic acid., Colloids Surf., B, 88 (2011) 108–114.

[40] P. Kanagaraj, A. Nagendran, D. Rana, T. Matsuura, Separation of macromolecular proteins and removal of humic acid by cellulose acetate modified UF membranes, Int. J. Biol. Macromol., 89 (2016) 81–88.

[41] K. Li, T. Huang, F. Qu, X. Du, A. Ding, G. Li, H. Liang, Performance of adsorption pretreatment in mitigating humic acid fouling of ultrafiltration membrane under environmentally relevant ionic conditions, Desalination, 377 (2016) 91–98.

[42] A. Matin, Z. Khan, S.M.J. Zaidi, M.C. Boyce, Biofouling in reverse osmosis membranes for seawater desalination: phenomena and prevention, Desalination, 281 (2011) 1–16.

[43] M.M. Clark, Transport Modeling for Environmental Engineers and Scientists, Second Edition, John Wiley & Sons, Hoboken, 2009.